Targeted perturbation of nuclear envelope integrity with vapor nanobubble-mediated photoporation

Targeted Perturbation of Nuclear Envelope Integrity with Vapor Nanobubble-Mediated Photoporation

Gaëlle Houthaeve[1,3†], Ranhua Xiong[2,3†], Joke Robijns[1], Bert Luyckx[4], Yasmine Beulque[4], Toon Brans[2,3], Coen Campsteijn[5], Sangram K. Samal[2,3], Stephan Stremersch[3], Stefaan C. De Smedt[3], Kevin Braeckmans[2,3*] and Winnok H. De Vos[1,4*]

[1] Laboratory of Cell Biology and Histology, Department of Veterinary Sciences, University of Antwerp, Antwerp, Belgium

[2] Centre for Nano- and Biophotonics, Ghent University, Ottergemsesteenweg 460, 9000 Ghent, Belgium

[3] Laboratory of General Biochemistry and Physical Pharmacy, Ghent University, Ottergemsesteenweg 460, 9000 Ghent, Belgium

[4] Cell Systems and Imaging Research Group (CSI), Department of Molecular Biotechnology, Ghent University, Ghent, Belgium

[5] Institute of Basic Medical Sciences, Department of Molecular Medicine, University of Oslo, PO box 1112 Blindern, 0317 Oslo, Norway

[†] Shared first authorship

[*] Shared senior authorship

Correspondence address: Prof. Winnok H. De Vos, Laboratory of Cell Biology and Histology, Department of Veterinary Sciences, University of Antwerp, Antwerp, Belgium

Abstract

The nuclear envelope (NE) has long been considered to only dismantle during mitosis. However, recent observations in cancer cells and laminopathy patient cells have revealed that the NE can also transiently rupture during interphase, thereby perturbing cellular homeostasis. Although NE ruptures are promoted by mechanical force and the loss of lamins, their stochastic nature and variable frequency precludes the study of their direct downstream consequences. We have developed a method based on vapor nanobubble-mediated photoporation that allows for deliberately inducing NE ruptures in a spatiotemporally controlled manner. Our method relies on wide-field laser illumination of perinuclear gold nanoparticles, resulting in the formation of short-lived vapor nanobubbles that inflict minute mechanical damage to the NE, thus creating small pores. We demonstrate that perinuclear localization of gold nanoparticles can be achieved after endocytic uptake or electroporation-facilitated delivery, and that both strategies result in NE rupture upon laser irradiation. Furthermore, we prove that photoporation-induced nuclear ruptures are transient and recapitulate hallmarks of spontaneous NE ruptures that occur in A-type lamin-depleted cells. Finally, we show that the same approach can be used to promote influx of macromolecules that are too large to passively migrate through the NE. Thus, by providing unprecedented control over nuclear compartmentalization, nuclear photoporation offers a powerful tool for both fundamental cell biology research and drug delivery applications.

Keywords: nuclear envelope, nuclear envelope rupture, nucleus, lamins, vapor nanobubbles, photoporation, gold nanoparticles

The nuclear envelope (NE) is a defining feature of eukaryotic cells. It shields the genetic content from the cytoplasm and thereby safeguards nuclear compartmentalization. The nuclear pore complexes (NPCs), which are embedded in the NE, allow tightly regulated transport between the nuclear interior and the cytoplasm. This is essential for genome maintenance and conditional gene regulation.[1,2] Directly underneath the NE resides the nuclear lamina, a network of filament-forming proteins, known as lamins.[3] Lamins regulate nuclear mechanics and play an important role in genome organization.[4-6] Their dysfunction is associated with a variety of disorders collectively referred to as laminopathies.[3]

Nuclear compartmentalization is temporarily lifted during mitosis when the NE is dismantled to allow segregation of duplicated DNA to the daughter cells. However, recent observations in laminopathy patient cells[7,8] and different types of cancer cells[9,10] have revealed that the NE can also rupture during interphase causing transient loss of nuclear compartmentalization. It is currently assumed that local mechanical force (*e.g.*, by compression or constricted migration)[10-12] is an important trigger for NE rupture (NER), and that NERs occur more easily at fragile sites of the NE, for instance, regions that are depleted from lamins.[8,10-11] Despite the severe impact on nuclear compartmentalization, cells are able to survive repetitive rounds of NER and retain their mitotic potential.[7,8] This implies efficient membrane resealing after NER, a feature that was recently attributed to the endosomal sorting complex required for transport (ESCRT-III) machinery.[8,10,12] Although NERs are transient, uncoordinated exchange of components between the nucleus and the cytoplasm could elicit persistent changes in signal transduction pathways and transcriptional programs.[7] Moreover, NERs result in the exposure of DNA to the cytoplasmic environment, which can cause DNA damage and provoke inflammatory auto-immune responses.[10,13,14]

Although some mechanistic insights have been obtained, the stochastic nature of spontaneous NERs precludes the study of their direct downstream consequences, such as

(repair) protein recruitment or adjoined ion fluxes, with high spatiotemporal resolution. Moreover, the low NER frequency in healthy cells makes it difficult to investigate NER mechanisms independent of a disease (*e.g.*, laminopathy) background. A solution to these problems is the controlled induction of NERs. A variety of tools has been developed to apply mechanical stress on cells and thereby evoke NERs. This includes confinement devices to compress single cells[15] or cell monolayers,[11,16] micropipette aspiration[17] or microfluidic channels with a cross-section that is smaller than the nuclear diameter for mimicking constricted migration.[10,12] Although these tools offer more control, they do not allow predicting exactly when and where NERs will take place. To achieve a more targeted NER induction, optical methods might offer a valid alternative. Direct illumination of the NE with a focused laser beam (*i.e.*, photoablation) has been shown to inflict damage to the NE,[10,12] but the approach has low throughput and, by definition, requires a high energy input. Both of these drawbacks can be eliminated using a modified laser technique such as vapor nanobubble (VNB)-mediated photoporation. This technique exploits the optical properties of sensitizing plasmonic nanoparticles such as gold nanoparticles (AuNPs) to significantly increase efficiency and throughput.[18-20] Absorption of a sufficiently intense, yet short (< 10 ns) laser pulse by an AuNP increases its temperature rapidly to several hundred degrees, causing the surrounding water to evaporate. This results in the formation of a quickly expanding VNB that, when it collapses, damages nearby biological structures by high-pressure shock waves. Owing to the extremely short lifetime and action radius of VNBs, the diffusion of heat from the AuNP into the surroundings is negligible, making VNB-mediated photoporation much less cytotoxic than photoablation.[18] Here, we show that VNB-mediated photoporation can indeed be used to temporarily perturb NE integrity. We found that AuNPs accumulate in the perinuclear region after endocytosis or electroporation-facilitated delivery, and that subsequent laser illumination results in the formation of VNBs close to the NE.

When applying this principle to a cell line that produces a nuclear-localized fluorescent protein, we measured a temporary shift in fluorescence signal to the cytoplasm, indicating transient permeabilisation of the NE. We also discovered that the same approach allows nuclear influx of macromolecules that are otherwise too large to passively migrate through the NE.

Results

AuNPs accumulate at the perinuclear region after endocytosis

Precise and efficient photoporation relies on the generation of VNBs around AuNPs in the vicinity of the target membrane. Hence, we first sought to enrich AuNPs at the NE. To this end, we exploited the cell's capacity to internalize cell-interactive AuNPs (coated with a cationic polymer) through endocytosis (Fig. 1a). HeLa cells were incubated with AuNPs for set periods of time (5 min, 1 h, 2 h, 6 h, 12 h and 24 h) (Fig. 1b). Quantification of the total number of AuNPs per cell revealed a progressive uptake with increasing incubation time, reaching a plateau after 6-12 h of incubation (Fig. 1c). Transmission electron microscopy (TEM) confirmed that the majority of the internalized AuNPs was located inside vesicles, consistent with endocytic uptake (Fig. 1d). Next, we calculated the number of perinuclear AuNPs as those particles lying within 1µm from the Hoechst-defined nuclear border (Fig. 1c, Fig. S5). At the early incubation times (up to 6 h, resp. 2 h), both the absolute and relative number of perinuclear AuNPs increased, pointing to a gradual enrichment of AuNPs at the perinuclear region. However, at longer incubation times, the number of perinuclear AuNPs did not increase any further. And, irrespective of the incubation time, more than 80% of the AuNPs were found throughout the cytoplasm, at significant distance (> 1 µm) from the NE. We reasoned that these distal AuNPs were not likely to contribute to NE pore formation and may provoke off-target damage upon VNB formation. Therefore, we sought to selectively reduce the distal AuNP fraction using a pulse-chase approach (Fig. S1a). Hereby, cells were incubated with AuNPs for a defined period of time (8h, pulse time), after which medium was exchanged and cells were further incubated in the absence of AuNPs for selected time periods (chase time). After quantification, we found that, prolonging the chase time did not lead to a selective enrichment of perinuclear AuNPs, but it did result in a significant reduction in the fraction of distal AuNPs, which could be important to minimize off-target

effects (Fig. S1b). Based on these results, we concluded that a pulse-chase approach with longer (24 h) chase time is the preferred strategy for nuclear photoporation experiments.

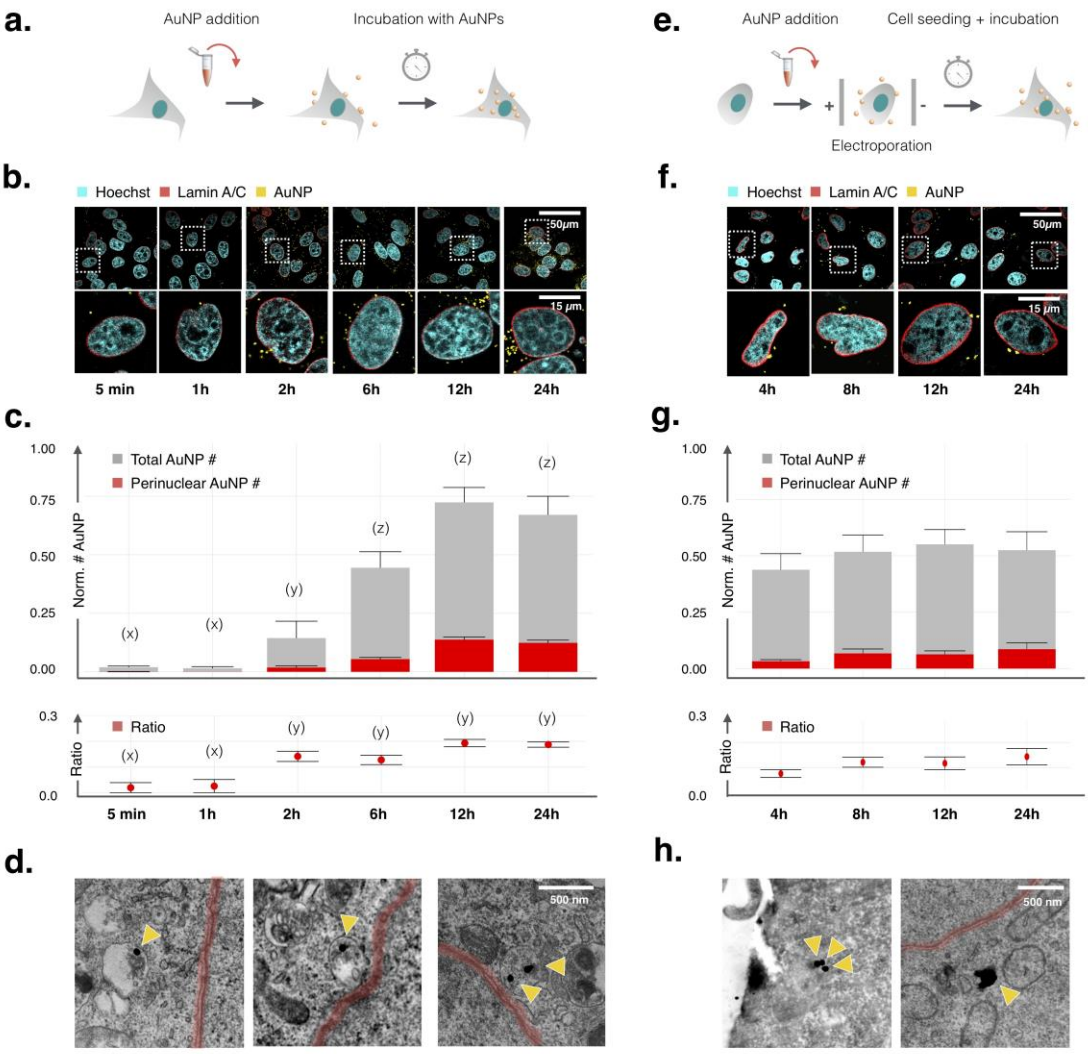

Figure 1. AuNPs partially accumulate in the perinuclear region after endocytic uptake (a-d) and after electroporation-facilitated uptake (e-h). (a) HeLa cells were continuously incubated with AuNPs and fixed after set time points (5 min, 1 h, 2 h, 6 h, 12 h, 24 h); (b) Representative images, acquired after immunostaining using a combination of confocal (lamin A/C, Hoechst) and reflection (AuNP) microscopy, and insets of individual nuclei are shown per time point; (c) The normalized number of total AuNPs (grey bars) and number of perinuclear AuNPs (red bars) per nucleus (± standard error) was automatically determined using an image analysis script (Suppl. Fig. 1). Perinuclear particles were defined as those lying at a distance < 1 µm from the nuclear border. The ratio of perinuclear AuNPs to the total number of AuNPs per nucleus is shown below as average ± standard error. Conditions that differ significantly (non-parametric multiple comparisons, significance

level p=0.05) are indicated by different lower-case letters (x, y and z); (d) Representative TEM images of HeLa cells, fixed 8 h after AuNP addition, showing individual AuNPs (yellow arrowhead) enclosed by an (endo-) membrane. To aid visualization, the NE has been manually delineated in red; (e) In a second approach, HeLa cells in suspension were incubated with AuNPs and electroporated, after which they were seeded in multi-well plates and allowed to reattach and spread for defined periods of time (4 h, 8 h, 12 h, 24 h); (f) Representative images, acquired after immunostaining using a combination of confocal (lamin A/C, Hoechst) and reflection (AuNP) microscopy, and insets of individual nuclei per time point; (g) The normalized number of total AuNPs (grey bars) and perinuclear AuNPs (red bars) per nucleus, and the ratio of both (average ± standard error). (h) TEM images of HeLa cells, fixed 8h after AuNP addition, showing groups of individual AuNPs or aggregates (yellow arrowhead), which are not enclosed by an (endo-)membrane. The NE has been manually delineated in red.

Electroporation allows delivery of non-encapsulated AuNPs

Spontaneous uptake results in sequestration of AuNPs inside endosomes (Fig. 1d). Since endosomal escape of AuNPs only occurs sporadically,[21] successful nuclear photoporation in such case demands simultaneous rupture of both the endosomal membrane and the NE. As this could lower the efficiency of the nuclear photoporation procedure, we explored whether AuNPs could be delivered directly into the cytoplasm by electroporation. We electroporated suspended HeLa cells in the presence of AuNPs and allowed the cells to reattach for defined periods of time (4 h, 8 h, 12 h, 24 h) (Fig. 1e-h). TEM showed that many AuNPs were not surrounded by a (endosomal) membrane, supporting a non-endocytic uptake pathway (Fig. 1h). However, both confocal reflection microscopy and TEM revealed the presence of larger clusters after electroporation-mediated delivery (Fig. 2f, d), as opposed to the individual, dispersed AuNPs witnessed after endocytosis-mediated delivery (Fig. 1b, d). We quantified the total number of AuNPs (or clusters) per cell after electroporation and found no significant change with incubation time (Fig. 2g). Unexpectedly, we also found a relatively consistent fraction (10%) of AuNPs in the perinuclear area (Fig. 2g). When including a medium

exchange step (pulse-chase, as performed for endocytic uptake), the total number of AuNPs per cell strongly decreased with increasing chase time, with variable, yet non-significant effects on the perinuclear AuNP fraction (Fig. S1c, d). We concluded that electroporation is capable of delivering AuNPs directly into the cytoplasm, some of which close to the NE, but this at the expense of their dispersed nature. Since AuNP aggregation could increase the extent of VNB formation, we reasoned that a minimization of the total AuNP number in this setting is crucial and thus a sufficiently long chase time is warranted.

Pulsed laser illumination of cells with perinuclear AuNPs results in VNB formation and subsequent NER

To verify whether VNBs can effectively be generated at cell-internalized AuNPs, their formation was visualized using dark field microscopy. AuNPs were delivered to the cells either *via* endocytosis (Fig. 2a) or electroporation (Fig. 2b) using a pulse-chase approach as described in the previous paragraphs. Irradiation with a short high intensity laser pulse resulted in the transient appearance of bright micron-sized dots, which vanished almost instantly (within a second), indicative of VNB formation.[18] Some VNBs located close to the nuclear border (Fig. 2, insets). Thus, we next assessed whether such perinuclear VNBs could exert sufficient force to permeabilize the NE.

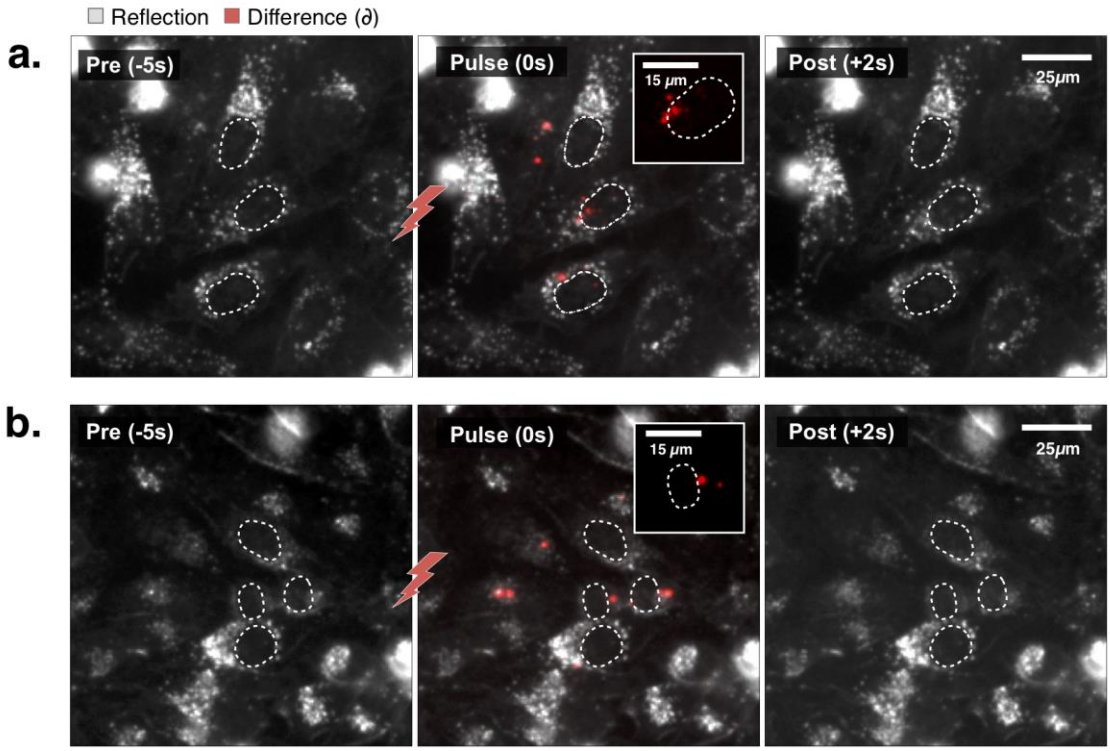

Figure 2. Perinuclear VNB formation. Dark field images of HeLa cells that have taken up AuNPs either by (a) endocytosis or (b) electroporation using a pulse-chase approach. Nuclei are indicated by dotted outlines; Irradiation with a short (< 10 ns) high intensity laser pulse (red bolt) results in the formation of VNBs, which appear as transient dots of bright light. To highlight these VNBs, darkfield images have been overlaid with a red-colored difference image (∂) of the images acquired just before and during laser illumination. Insets show the difference image of selected nuclei, thus showing only the VNBs, some of which close to the nuclear border. Directly (within seconds) after laser illumination, VNBs have vanished.

Permeabilisation of the NE can be visualized in cells producing exclusively nuclear-localized fluorescent proteins as a reduction in nuclear signal intensity and concurrent increase in cytoplasmic intensity (Fig. 3a). Hence, we generated a stable HeLa cell line that produces a GFP fused to a nuclear localization signal (NLS). We further refer to this cell line as HeLa-NLS-GFP. After (endocytic or electroporation-mediated) AuNP delivery and 24 h chase time, HeLa-NLS-GFP cells were visualized using confocal microscopy. As expected, all cells showed strong fluorescence in the nucleus and faint signal in the cytoplasm. When cells were

subsequently irradiated with nanosecond laser pulses with a fluence of 0,8 J/cm^2, several cells showed an instant strong drop in nuclear intensity and modest increase in cytoplasmic intensity, as compared to their pre-photoporation state, suggesting successful NE permeabilisation (Fig. 3b). Control cells that were not incubated with AuNPs, but which were irradiated with the same laser intensity did not show this phenomenon (Fig. 5a). Cross-comparison with reflection microscopy images acquired prior to photoporation, showed that those cells demonstrating loss of nuclear compartmentalization originally had one or more perinuclear AuNP(s), suggesting a VNB-mediated effect (Fig. 3c). Manual quantification revealed that the efficiency of nuclear photoporation at the cell population level was 6-7% with no significant difference between endocytic and electroporation-facilitated AuNP delivery (Fig. 4a). More importantly, live cell imaging revealed that the loss of nuclear compartmentalization was not permanent, since nuclear signals were found to restore after successful nuclear photoporation (Fig. 3c). Of those cells that were successfully photoporated, 82% recovered their nuclear signal within 1 h after endocytic AuNP delivery, and 68% after electroporation-facilitated AuNP delivery (Fig. 4b). To ascertain whether the capacity to undergo transient nuclear ruptures was not limited to transformed HeLa cells, we also tested the nuclear photoporation procedure on a non-transformed cell line, namely the retinal pigment epithelial cell line RPE-1, which was lentivirally transduced with a fluorescent reporter coupled to a nuclear export sequence (mRuby3-NES). Whereas under basal conditions mRuby3-NES was sequestered in the cytoplasm, we observed a transient entry of the fluorescent protein into the nucleus (and concurrent increase in N/C signal ratio) upon successful nuclear photoporation (Fig. S2). Thus, we conclude that VNB-mediated nuclear photoporation is feasible in different cell types after both electroporation-mediated as well as endocytic AuNP delivery.

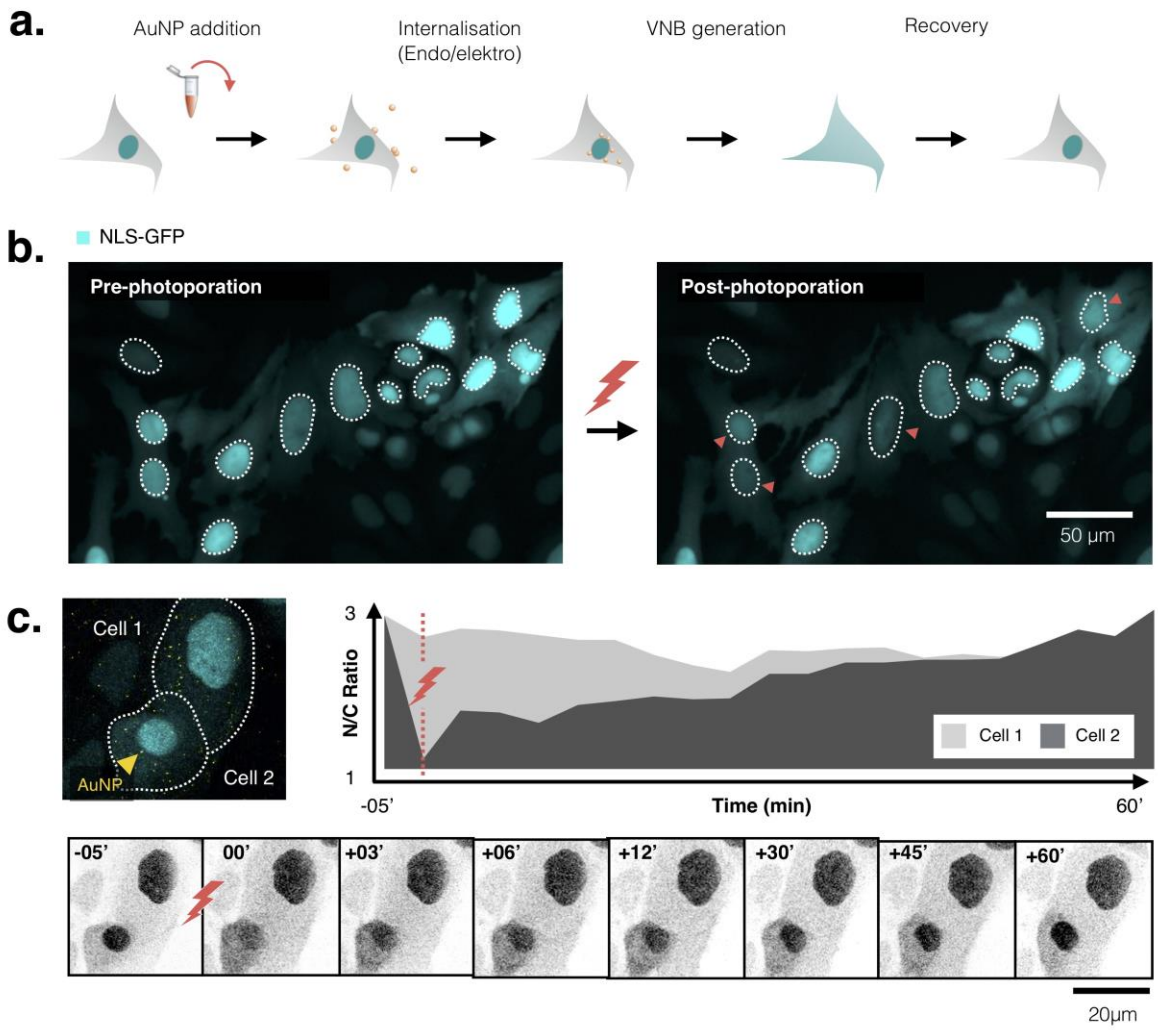

Figure 3. Nuclear photoporation elicits transient ruptures of the NE. (a) Schematic illustration of the nuclear photoporation workflow: AuNPs were added to HeLa-NLS-GFP cells (endocytosis- or electroporation-mediated delivery) allowing their uptake and perinuclear accumulation. After 8 h incubation the medium was exchanged. The next day, cells were irradiated with a pulsed laser thereby inducing localized VNB formation. In those cells that have perinuclear AuNP(s), this leads to temporary NE perforation causing leakage of nuclear NLS-GFP to the cytoplasm. Upon resealing of the NE, NLS-GFP restores its nuclear localization; (b) Example of HeLa-NLS-GFP cells before and after photoporation. Red arrowheads indicate successful nuclear photoporation events; (c) Example of successful nuclear photoporation with recovery of nuclear compartmentalization: only in cell 2, which has a perinuclear AuNP (yellow arrowhead), a temporary loss of nuclear compartmentalization is observed after photoporation (red lightning bolt), as evidenced by the transient reduction in nuclear-to-cytoplasmic signal ratio (N/C ratio). Cell 1, which has no perinuclear AuNP, does not show this event nor change in N/C ratio after laser illumination. The grayscale range of the time montage has been inverted for clarity.

Cells can retain their proliferative capacity after nuclear photoporation

To obtain a rough estimate of the impact of the photoporation procedure on cell viability (regardless of the efficiency to permeabilize the NE), we measured metabolic activity (ATP levels) 2 h and 24 h after laser treatment, relative to samples that had not been incubated with AuNPs (Fig. 4c). 2 h after laser treatment, viability percentages for endocytic AuNP uptake and electroporation-mediated AuNP uptake were similar (74% resp. 75%), while 24 h after laser treatment, cells that had been subjected to endocytic AuNP uptake showed lower viability percentages than cells subjected to electroporation (54% resp. 73%). Part of the adverse effect could be explained by factors not related to the photoporation itself, since cell cultures that were incubated with AuNPs but which were not exposed to laser illumination already showed a decrease in cell viability 2 h (81%, for endocytosis, 70% for electroporation) and 24 h (87%, for endocytosis, 70% for electroporation) after mock treatment, as compared to non-treated controls.

We next asked what the exact contribution of nuclear photoporation was to the observed reduction in cell viability. A propidium iodide (PI) staining 30 min after photoporation showed that none of the cells that had undergone successful photoporation were positive for PI. This suggests that nuclear photoporation is not associated with simultaneous damage to the plasma membrane (Fig. 4d). However, when comparing images acquired prior to and immediately after laser treatment, we consistently found a small fraction of cells (~5%) in which the NLS-GFP signal had vanished completely. It is plausible that these cells may have been excessively photoporated and were therefore lost immediately after laser illumination (Fig. 4a, e). Incubation of cells with PI 6 h after photoporation, revealed that some cells did become PI positive, pointing to the induction of a cell death pathway. But, this feature was observed in cells that had undergone successful nuclear photoporation as well as in cells that had not (Fig. 4e, Fig. S3). More importantly, many of the photoporated cells were PI

negative, indicating that nuclear photoporation is not necessarily toxic (Fig. 4e, Fig. S3). On the contrary, when following up cells for 24 h after laser exposure, we found several cells to divide after successful nuclear photoporation (Fig. 4f, Fig. S4; Movie S4). Thus, cells can recover and even maintain their proliferative capacity after nuclear photoporation.

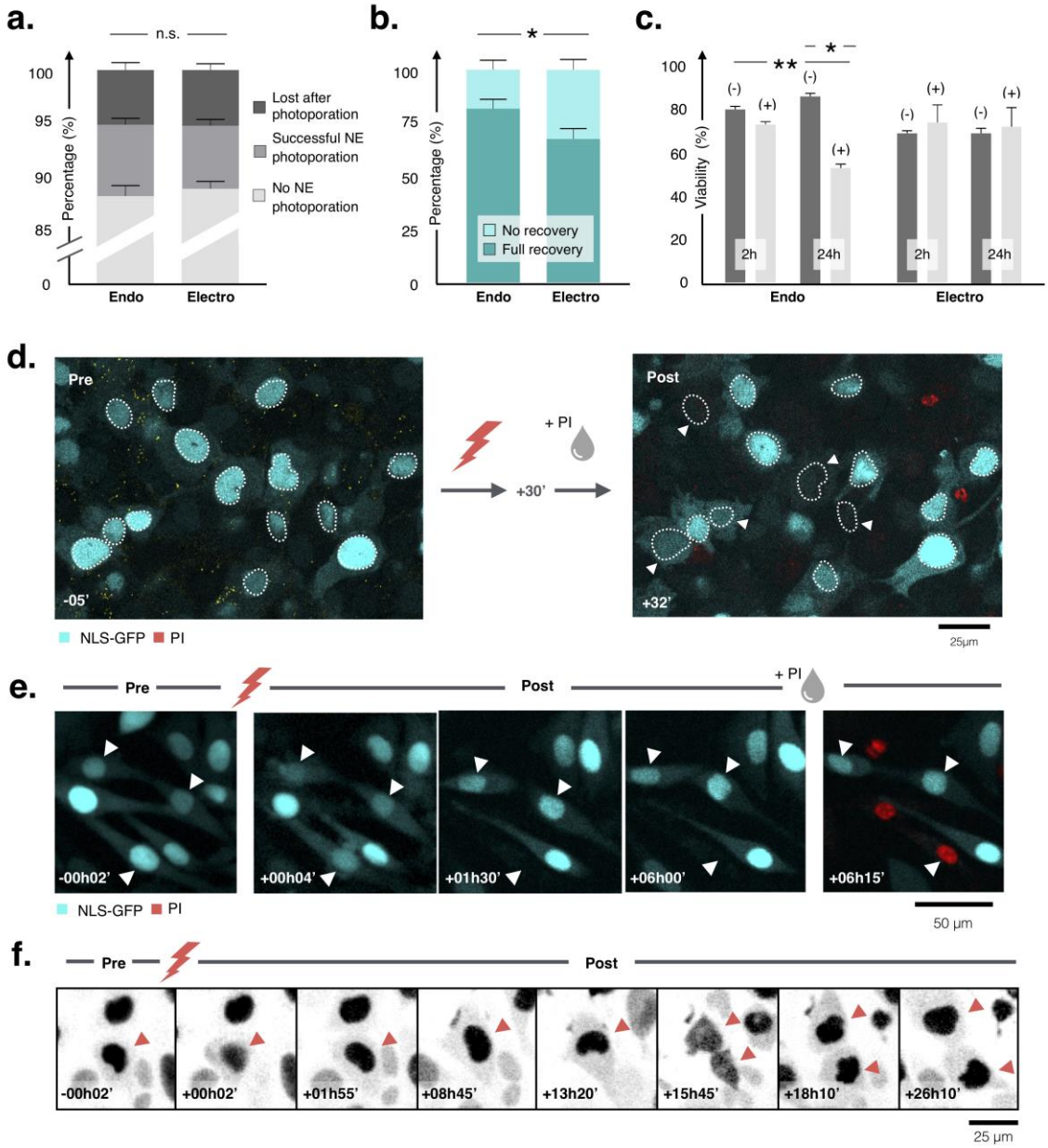

Figure 4. HeLa cells can survive nuclear photoporation and are able to maintain their proliferative capacity. (a) Comparison of the percentage of successfully photoporated cells for endocytic and electroporation-facilitated AuNP delivery as determined by leakage of NLS-GFP signal out of the nucleus; (b) Comparison of the percentage of cells that recover completely after nuclear photoporation for endocytic and

electroporation-facilitated AuNP delivery (p=0.02, Mann-Whitney test); (c) Viability after photoporation as determined by Cell-Titer Glo assays 2 h (left) and 24 h (right) after laser treatment for endocytic and electroporation-facilitated AuNP delivery. Bar graphs represent the percentage of viable cells expressed relative to the control condition (without AuNPs), for mock treatment (-) and laser treatment (+) (* p=0.0025; ** p=0.017; Post-hoc test with Bonferroni correction for multiple testing); (d) Representative confocal microscopy images of HeLa-NLS-GFP cells 2min before (left) and 32 min after (right) laser treatment. Propidium iodide (PI) was added 30 min after laser treatment; (e) Montage of HeLa-NLS-GFP cells monitored for 6h after laser treatment to monitor recovery of nuclear signal after nuclear photoporation, and subsequent addition of PI (at 6 h post exposure) to visualize dead (red) cells; Both PI-positive and PI-negative cells are observed; (f) Montage of a HeLa-NLS-GFP cell undergoing cell division after successful nuclear photoporation (see also Movie S4). The grayscale range of the time montage has been inverted for clarity.

Nuclear photoporation recapitulates features of spontaneous NERs

The recovery of nuclear NLS-GFP showed that nuclear photoporation causes a transient loss of nuclear compartmentalization (Fig. 3c, Movies S1-3). To quantitatively compare the recovery kinetics after nuclear photoporation with endocytic or electroporation-mediated AuNP delivery, we made use of a previously established method to synchronize spontaneous NERs *in silico*.[8] A striking similarity was found between the average recovery profiles of cells that had undergone successful nuclear photoporation after endocytic or electroporation-mediated AuNP delivery, with an average recovery halftime ($T_{1/2}$) in between 20 - 25 min (Fig. 5b). For comparison, we also measured the recovery kinetics of spontaneous NERs in newly made *LMNA* knockout HeLa cells. We chose these cells because of their strongly increased NER propensity.[7-9] We found that the initial recovery after spontaneous NERs ($T_{1/2}$ = 10 min) was faster than after nuclear photoporation (Fig. 5b). However, in line with spontaneous NERs that have been observed in cancer cells undergoing confinement[16] or constricted migration,[10,16] we could detect local lamin depositions (*i.e.*, lamin scars) at the site of rupture (Fig. 5c). Furthermore, using a mutant version (with abolished enzyme activity) of

the cytosolic DNA-binding protein Guanosine 3′,5′-monophosphate–adenosine 3′,5′-monophosphate (cyclic GMP-AMP) synthase (cGAS), fused to Red Fluorescent Protein (RFP),[22] we found that nuclear photoporation was accompanied by the exposure of unprotected chromatin to the cytoplasm (Fig. 5d).

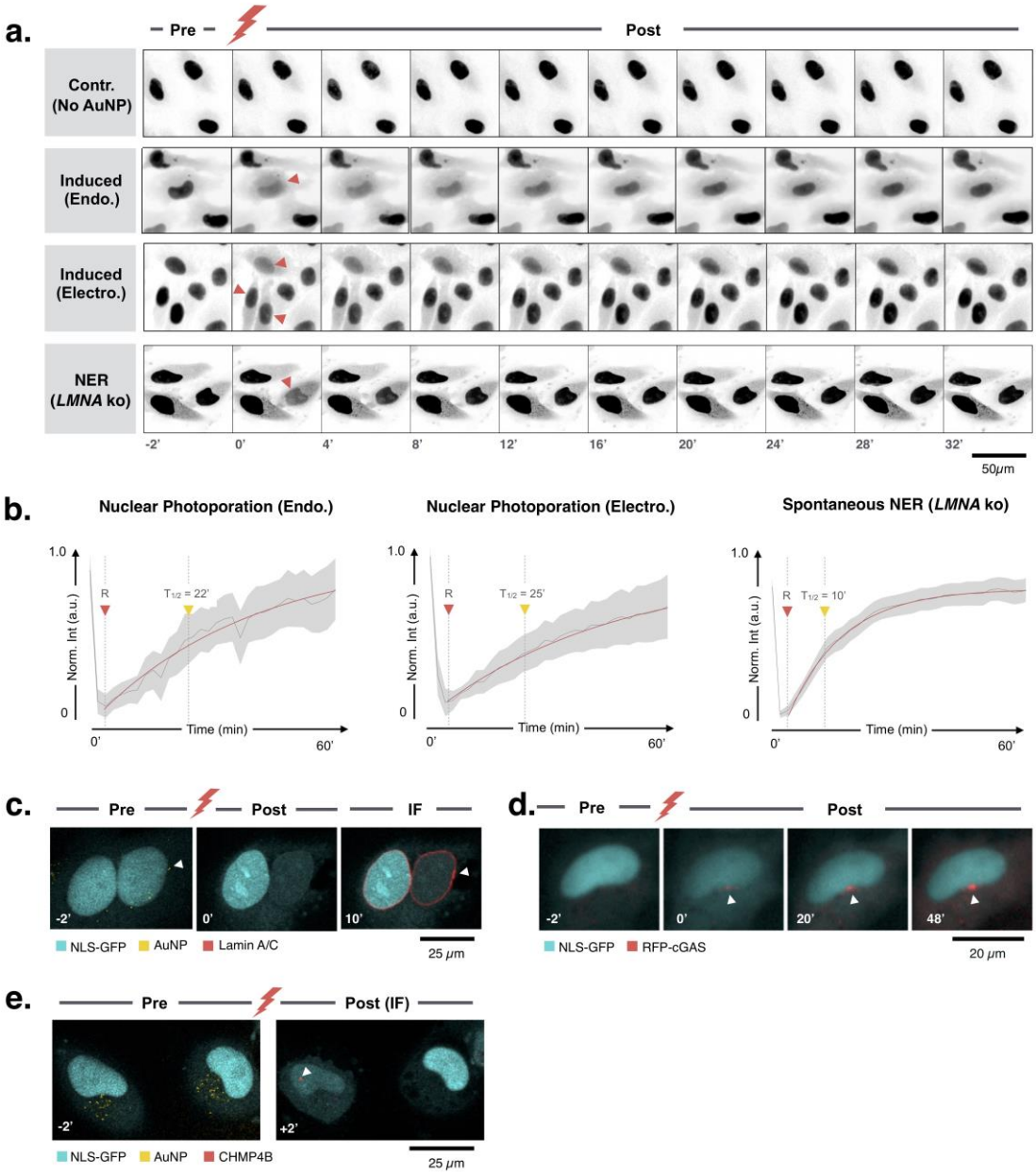

Figure 5. NE repair kinetics after nuclear photoporation are comparable between both AuNP administration methods (endocytosis or electroporation) and mimic in part the NE repair kinetics after spontaneous rupture. Stable HeLa-NLS-GFP cells or transiently transfected *LMNA* knockout cells were followed up to one hour after nuclear photoporation, resp. spontaneous NER. (a) Images of representative ruptures of every condition are

shown starting from right before (pre-) rupture to 32 min after (post). The grayscale range of the time montage has been inverted for clarity. The (VNB-induced or spontaneous) rupture point is indicated with a red lightning bolt, and successful ruptures are indicated by red arrowheads; (b) Normalised (to the average) nuclear signal intensity of HeLa-NLS-GFP cells that undergo induced ruptures or *LMNA* knockout (ko) HeLa cells that undergo spontaneous NERs plotted as a function of time after *in silico* synchronization (average with 95% t-distribution based confidence interval). From left to right: nuclear photoporation after endocytic AuNP delivery (n = 11 cells), nuclear photoporation after electroporation-mediated AuNP delivery (n = 13 cells) and spontaneous NERs in *LMNA* ko cells (n = 32 cells). Rupture points (R) and recovery half-times ($T_{1/2}$) are indicated per plot; (c) Formation of a lamin scar at the site of a perinuclear AuNP after nuclear photoporation (arrowhead), as revealed by post-hoc immunofluorescence (IF) staining; (d) Nuclear photoporation is accompanied by the cytoplasmic exposure of genomic DNA at the site of rupture (arrowhead) as visualized by RFP-cGAS relocalization. Cytosolic background signal may be due to the overexpression or detection of superfluous plasmid in the cytosol; (e) Recruitment of the NE repair factor CHMP4B to the ruptured NE as revealed by post-hoc immunofluorescence (IF) staining.

Finally, CHMP4B (a component of the endosomal sorting complexes required for transport-III (ESCRT-III) machinery involved in NE repair)[10,12] was sometimes observed to be recruited specifically to the NE of ruptured nuclei (Fig. 5e). Thus, photoporation-induced NE permeabilisation shares features with spontaneous NERs as observed in A-type lamin depleted cells.

Nuclear photoporation leads to nuclear influx of exogenous fluorescent dextran

Experiments with HeLa-NLS-GFP cells revealed that nuclear photoporation caused a temporary loss of nuclear compartmentalization. Hence, we asked whether this approach could also be used to bring extraneous macromolecules into the nucleus that are normally too large to spontaneously pass through the nuclear pore complexes. As a model marker, we selected FITC-labeled dextran of 70 kDa (FD70), which is a relatively inert molecule that is normally excluded from the nucleus.[7] Cells were first loaded with FD70 in their cytoplasm

using standard photoporation of the plasma membrane (as optimized before[18], Fig. 6a). This resulted in the majority of the cells showing strong fluorescent signal in the cytoplasm and faint signal in the nuclei (Fig. 6b). Next, we allowed cellular uptake and perinuclear accumulation of AuNPs to allow for subsequent nuclear photoporation. To avoid nuclear entry of FD70 during mitosis, we shortened the pulse and chase time (to 4 h, resp. 1 h). Fluorescence images taken directly after the nuclear photoporation laser pulse, showed that laser treatment had resulted in a significant increase in the number of cells with nuclear fluorescence (Fig. 6b, c, e). Successful nuclear photoporation was also reflected by a significant rise in the nuclear-to-cytoplasmic fluorescence signal ratio across the cell population (Fig. 6d, Fig. S6). A similar experiment revealed that nuclear loading could also be achieved after sequential plasma membrane and nuclear photoporation with the larger dextran variant of 150 kDa (FD150) (Fig. 6f). Therefore, we conclude that nuclear photoporation allows the bidirectional exchange of molecules that are larger than the NE exclusion limit.

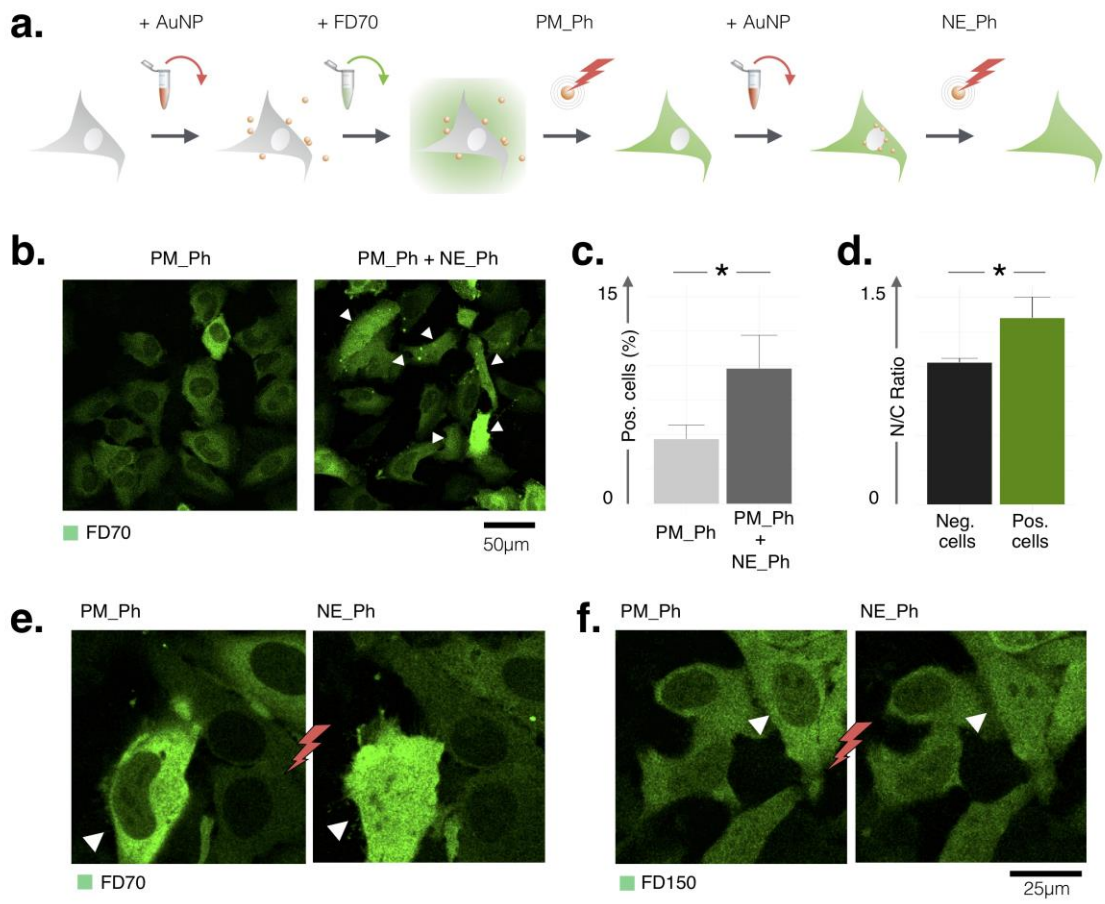

Figure 6. Nuclear photoporation allows intranuclear loading of extraneous FITC-dextran. (a) Schematic illustration of the workflow: First AuNP-mediated photoporation was performed at the level of the plasma membrane (PM_Ph) to load the cytoplasm of the cells with 70 kDa FITC-dextran (FD70). Next, cells were pulse-chase incubated with AuNPs to allow for endocytic uptake and perinuclear accumulation of AuNPs. Finally, nuclear photoporation was executed (NE_Ph) to load the FD70 into the cell nuclei; (b) Representative images of cells that have undergone only plasma membrane photoporation or plasma membrane photoporation followed by nuclear photoporation. Cells with nuclear-loaded FD70 are indicated by arrowheads; (c) Plasma membrane photoporation followed by nuclear photoporation (n = 383 cells) significantly (p=0.039, Mann-Whitney test) increases the number of cells with nuclear FD70 loading, and (d) significantly (p=3,45 E-11, Mann-Whitney test) raises the nuclear-to-cytoplasmic (N/C) signal ratio as compared to plasma membrane photoporation alone (n = 412 cells); (e) Enlarged region of a confocal field, pre- and post-nuclear photoporation showing entry of FD70 into the nucleus of a HeLa cell upon successful nuclear photoporation (arrowhead); (f) Enlarged region of a confocal field showing nuclear entry of FD150 after nuclear photoporation (arrowhead).

Discussion

We have demonstrated that VNB-mediated photoporation, a technique originally developed for permeabilisation of the plasma membrane,[18] can also be used to permeabilize the NE. Using cells that stably express a free floating nuclear reference marker (NLS-GFP), we showed that laser irradiation causes the fluorescent reporter to leak out of the nucleus specifically in those cells that have accumulated one or more perinuclear AuNPs. Further, we found that the photoporation-induced loss of nuclear compartmentalization was transient, similar to spontaneous NERs in A-type lamin-depleted cells. Moreover, hallmark NER features such as the formation of lamin scars and cytoplasmic chromatin exposure were documented after nuclear photoporation. Thus, our approach may be used to study the downstream consequences of (induced) NER with high spatiotemporal resolution. We also showed that VNB-mediated nuclear photoporation can facilitate nuclear influx of exogenous molecules that are otherwise too large to spontaneously pass through the nuclear pore complexes.[23] More specifically, we found both 70 kDa as well as 150 kDa FITC dextran to enter the nucleus after nuclear photoporation. Considering the estimated diameter of these molecules (11,1 nm, resp. 16,6 nm), we conclude that the size of the induced pores must be larger than 10 nm. Hence, the approach could find its use in therapeutic applications as well, for instance for the delivery of (macro-)molecules to the nucleus of post-mitotic cells,[24] such as expression plasmids or large nucleases that are typically used for genome editing.[25]

A limitation of the current approach is that the efficiency of nuclear photoporation is rather low. As we initially reasoned that this could be due to the sequestration of AuNPs in endosomes,[26] we investigated whether electroporation could be used to deliver AuNPs directly into the cytoplasm. We found that electroporation was able to do so, and effectively circumvented endosomal sequestration, but this at the expense of their dispersed character. Moreover, the efficiency of nuclear photoporation after electroporation-mediated delivery

was not higher than that obtained after endocytic delivery. We therefore speculate that the presence of an extra membrane (*i.e.,* the endomembrane) does not have a major impact on the capacity to induce NERs. Rather, the heterogeneity of intracellular AuNP distributions within a cell population seems the prime determinant. Although we have selected conditions that resulted in a minimal number of distal particles, population-based biochemical measurements also revealed a decrease in viability for both approaches. Part of this reduction could be explained by the experimental conditions, which are not related to the actual photoporation procedure (such as AuNP delivery), but we cannot exclude additional off-target damage originating from VNBs at non-perinuclear sites. Especially endocytic uptake resulted in a significant decrease in viability 24 h after delivery. We speculate that this may be caused by rupture and subsequent leakage of (endo)lysosomes that enclose the internalized AuNPs. Thus, endocytic AuNP uptake may not be the preferred strategy for nuclear photoporation. Improving the efficiency and specificity of photoporation will demand maximizing the number of cells with perinuclear AuNPs, whilst further reducing the number of distal AuNPs. One solution could be to combine electroporation-mediated delivery with specific functionalization of the AuNPs so as to target them to the NE. Targeting molecules that could be of interest in this context include signal peptides such as the nuclear localization signal (NLS)[27] or nanobodies that recognize epitopes of NE-specific proteins (*e.g.*, cytoplasmically oriented nucleoporins, such as Nup82)[28]. Although electroporation facilitated direct AuNP delivery into the cytoplasm, we noticed that the procedure correlated with the presence of AuNP clusters. It will have to be investigated whether aggregation interferes with targeted transport to the NE, and whether additional functionalization such as PEGylation might alleviate this issue.[29]

With the current protocol, a substantial fraction of cells survived successful nuclear photoporation, restored nuclear compartmentalization and even maintained their replicative

potential. Quite surprisingly, a strong similarity was observed in average recovery profiles for both AuNP delivery methods. This suggests that the damage inflicted to the NE is of comparable magnitude and/or that there is a common and very effective repair pathway. The lower capacity of cells to restore nuclear compartmentalization on the short term (up to 1 h after photoporation) after electroporation-mediated AuNP delivery might be due to the higher variability in VNB size (and consequent NE pore size) of AuNP aggregates.[30] It is conceivable that with increasing pore size, nuclear compartmentalization takes longer to restore, and that above a certain threshold level of damage (pore size), it may even no longer be restored at all. Why the (especially initial) recovery occurs faster after spontaneous NERs is unclear, but it may depend on differences in physicochemical properties of the pores, such as size and type, that trigger different repair pathways.[31] Cell-type specific differences in sensitivity to NER or differences in nuclear transport efficiency between lamin-positive *versus* lamin-depleted cells may contribute as well to the difference in repair kinetics. Finally, lamin-depleted cells may be more primed for repair and recovery because of the frequent occurrence of NERs.[32]

Conclusion

To conclude, we have developed a method that allows inducing NERs with high spatiotemporal control in different cell types independent of their genetic background. In this technique, mechanical shockwaves originating from VNB-collapse are responsible for transient rupture of the NE. The induced ruptures recapitulate features of the spontaneous nuclear ruptures observed in laminopathy patient cells. To increase the efficiency of the nuclear photoporation technique further, specific and selective NE targeting strategies for AuNPs should be conceived. This way, nuclear photoporation may also become an attractive tool for boosting nuclear delivery.

Materials and Methods

Cell culture

The human cervix carcinoma cell line *HeLa* and its genetic derivatives clones HeLa-NLS-GFP and HeLa *LMNA* knockout (*LMNA* ko) were cultured in Dulbecco's Modified Eagle Medium (DMEM) supplemented with L-glutamin (Lonza, BE12-604F/12), 10% fetal bovine serum (Gibco, 10270-106), and 1% penicillin/streptomycin (Gibco, 15140-122), according to standard procedures. The retinal pigment epithelial (RPE-1) cell line (constitutively expressing 2xmRuby3-NES) was cultured in DMEM F-12 Nutrient Mixture (Ham) supplemented with L-glutamin (Lonza, BE12-604F/12), 10% fetal bovine serum (Gibco, 10270-106), and 1% penicillin/streptomycin (Gibco, 15140-122), according to standard procedures. Proliferative capacity was monitored by cell counting with every passage and cultures were tested for mycoplasma infection using a PCR test kit (Bio-connect, PK-CA91-1024) every two months. For imaging and photoporation, cells were either grown on glass bottom dishes (Greiner Bio-One, 627860) or in 96-well glass bottom microplates (Greiner Bio-One, 655892) in complete medium supplemented with 25 mM HEPES (to buffer for CO_2 fluctuations).

Transient and stable transfection

Cells were transiently transfected with the construct NLS-GFP or RFP-cGAS using Lipofectamin 2000 (Life Technologies, 11668027) according to the manufacturer's instructions. To establish stable reporter cell lines we followed a protocol essentially described before.[33] In brief, the workflow consists of growing transiently transfected cells for two weeks in the presence of 500 µg/ml G418 antibiotic, followed by sorting of individual positive cells *via* fluorescence-activated cell sorting (FACS) into 96-well plates and expansion to single cell colonies that stably produce the fluorescent reporter. The RPE-1

mRuby3-NES cell line was generated using lentiviral transduction leading to stable EF1α-promoter driven expression of the Rev NES fused to tandem copies of mRuby3. The *LMNA* ko cell line was generated using CRISPR-Cas9 technology with a gRNA targeting the first exon of the LMNA gene (5'-CCTTCGCATCACCGAGTCTGAAG-3') as described before.[8] Plasmids were from Addgene (#48138 and 48139) and protocols were followed as described in Ran *et al*., 2013.[34]

Photoporation

A homemade setup including an optical system and electric timing system was used for photoporation.[18] A pulsed laser with pulse duration of ~7 ns was tuned at a wavelength of 561 nm (Opolette HE 355 LD, OPOTEK Inc., CA, USA) and used for illumination of AuNP. An electronic microscope stage was used to scan the laser beam (20 Hz pulse frequency) line by line across the sample. The scan speed was 1,6 mm/s, and the distance between subsequent lines was 0.08 mm (a bit smaller than the diameter of the laser beam, which is 0.12 mm to generate partial overlap). During scanning, a laser intensity of 40 μJ was used, which corresponds to a laser fluency of ~ 0,778 J/cm^2. The laser pulse energy was monitored by an energy meter (J-25MB-HE&LE, Energy Max-USB/RS sensors, Coherent) synchronized with the pulsed laser.

For photoporation at the level of the plasma membrane, HeLa cells were incubated with cationic AuNP of 70 nm (NanoPartz #C2159, Nanopartz Inc., Loveland, CO, USA) for 30 min at a concentration of 4 E+07 AuNPs/ml. Following incubation with AuNPs, the cells were gently washed to remove any remaining free AuNPs in solution and medium was added containing 70 kDa or 150 kDa FITC-labeled dextran (FD70 or FD150, Sigma-Aldrich). After photoporation, cells were washed and medium was replaced with fresh medium.

For photoporation at the level of the NE, cells were incubated with 2.5 E+08 AuNP/ml AuNP

and incubated for set time points after endocytic or electroporation-mediated delivery. After nuclear photoporation, cells were either fixed and (immuno-) stained, or followed up with live cell time-lapse imaging. In the latter case, before photoporation, cells were first localized using a fluorescence widefield microscope (Nikon TE2000, Nikon Instruments). The coordinates of these regions were saved and directly after photoporation, regions were revisited to acquire images for 60 min at 2-3 min intervals.

Electroporation

Electroporation was used to load AuNP into cells. HeLa cells were suspended using trypsin and resuspended in OptiMEM (Life Technologies) at an approximate concentration of 2.25 E+06 cells/ml. AuNP were diluted in OptiMEM down to a concentration of 2 E+09 AuNP/ml. Electroporation cuvettes (4mm, VWR International, Belgium) were filled with cell suspension and AuNP solution at a 2:1 ratio (total volume of 300 µl). After mild vortexing, the cuvettes were placed in a Bio Rad Gene Pulser® II and electroporated using a voltage difference of 125V and a capacitance of 125µF. For internalization studies, directly after electroporation cells were seeded in 96-well glass bottom microplates containing 150 µl pre-warmed DMEM per well and placed in the incubator to allow reattachment. After fixed time points, cells were used for photoporation. Subsequently the cells were fixed with 4% paraformaldehyde, followed by immunostaining.

Viability assays

CellTiter-Glo® Luminescent Cell Viability Assay (Promega) was performed on HeLa-NLS-GFP cells in 96-well plate format according to the manufacturer's standard protocol. In short, cell medium was exchanged and an equal amount (100 µl) of the CellTiter-Glo® reagent was added to every well. Afterwards, the plate was transferred to an orbital shaker to mix the

contents so as to induce cell lysis (10 min at 120 rpm). Finally, 100 µl of every well was transferred to a white opaque plate for luminescence measurements, reporting on population-level viability.

For single cell viability assessment, propidium iodide (PI) (ThermoFisher Scientific) was added to the cells in glass bottom dishes to a final concentration of 1 µM, either 30 min after laser treatment, or 6 h after laser treatment. Cell were incubated at 37° C for 15 min. before images were acquired with a fluorescence microscope.

Immunofluorescence

Cells were fixed with 4 % paraformaldehyde for 15 min followed by 3 × 5 min wash steps with PBS (Life technologies, 14190-169). After permeabilisation in 0.5 % triton X-100 for 5 min and blocking for 30 min, primary antibody (mouse anti-lamin A/C, Abcam, ab26300, 1/1000) was added for 1 h. After 3 × 5 min wash steps with PBS, secondary antibody (donkey anti-mouse Alexa Fluor 647, Jackson, 705606147, 1/300) was added for 1 h. After an additional series of wash steps, DAPI (1 µg/ml) or Hoechst (2 µg/ml) was added for 10 min to the cells and slides were mounted with Vectashield (Vector Labs) or after additional washing the plates were kept in PBS at 4 °C for microscopy.

Microscopy

Time-lapse imaging on HeLa *LMNA* ko cells was performed on a Perkin Elmer Ultraview Vox dual spinning disk confocal microscope, mounted on a Nikon Ti body, equipped with a Perfect Focus System and a microscope incubator equilibrated at 37 °C. Recordings were made every 2–3 min, using a 20×/0.75 Plan Achromat dry lens. Image acquisition was done using Volocity software. Per compartment, 10 regions were monitored, allowing acquisition of 40 different regions in a 2 min time frame. Care was taken to only select cells with

moderate expression levels and correct (initial) localization patterns. Cellular condition was also verified by phase contrast microscopy, to assure that cells showed a normal morphology without excessive vacuole formation.

For time-lapse imaging after nuclear photoporation, glass bottom dishes with HeLa-NLS-GFP were transferred from the epifluorescence microscope (Nikon TE2000, Nikon Instruments) to a spinning disk microscope (Yokogawa CSU-X), equipped with an EM-CCD camera (Andor, iXon ultra 897) and laserbox from Aligent Technologies (MLC, 400B). To retrieve the same regions, stage calibration was done between both microscopes, based on the coordinates of 3 reference points. Recordings were made every 2-3 min, using a 20x/0.75 Plan Achromat dry lens. Image acquisition was done using NIS elements AR. Per glass bottom dish, (consisting of one compartment) 49 regions were monitored up to 24 h.

Pre- and post-photoporation localization and immunofluorescence staining were visualized using a Nikon C1 microscope (Nikon Instruments) with a 60x/1.4 Plan Apo VC oil objective or 60x/1.2 Plan Apo VC water immersion objective. Hoechst and DAPI were exited with a 408 nm solid state laser and detected through a 440/40 nm emission filter; GFP was excited with a 488 nm solid state laser and detected through a 515/30 nm or 525/50 nm emission filter; Alexa647 was excited with a 633 nm solid state laser and detected through a 660 nm long-pass emission filter. AuNPs were visualized with the 561nm laser line, using an 80/20 beam splitter and no emission filter.

Image Analysis

To quantify the internalization of AuNPs, a script was written for FIJI image analysis freeware (http://Fiji.sc) that determines the distance of individual AuNPs to the nucleus (Dist2Nuc.ijm, available upon request, Fig. S5). In brief, the workflow consists of nuclei detection, spot detection and distance measurement. Nuclei are detected in maximum

projections of confocal Z-stacks of the DAPI/Hoechst channel after local contrast enhancement and Gaussian smoothing to respectively cover for spatial illumination heterogeneity and noise. After automatic thresholding (Isodata algorithm), touching nuclei are separated using a conditional watershed algorithm. AuNPs are detected in the reflection channel using a Laplacian of Gaussian blob detector (scale = 1σ) and binarized using an automatic threshold algorithm (Triangle algorithm). Individual AuNP objects are saved as a list of regions of interest (ROIs). To determine the closest distance of the detected AuNPs to every nucleus in the field of view at once, the binary mask of detected nuclei is converted into a Euclidean Distance Map and the minimum value (*i.e.*, distance) is measured per object for the entire AuNP ROI set. A second script was used to quantify a shift in the nuclear-to cytoplasm signal intensity ratio (Fig. S6). In brief, this analysis segments nuclei and uses the nuclear mask to define a perinuclear cytoplasmic region by conditional (*i.e.*, Voronoi-restrained) region growing. Subsequently the average intensity of the molecular marker channel (FD70, NLS-GFP) is measured in both the nuclear and cytoplasmic ROIs and the ratio is calculated per cell. Finally, a third script (trackRuptures.ijm), written for FIJI image analysis freeware (http://Fiji.sc), was used to automatically track nuclei and measure their signal intensity (NLS-GFP) through time. For a detailed explanation of this script we refer to Robijns *et al*., 2016.[8]

Acknowledgements

This research was supported by the University of Antwerp (TTBOF/29267, BOF/30112 and BOF/33280), the Special Research Fund of Ghent University (BOF/11267/09; 01-MR0110), the European Research Council (ERC, 648124), and the Research Foundation Flanders (FWO, 1152918N). I. Pintelon is gratefully acknowledged for her assistance during TEM experiments (University of Antwerp) and N. Cools (University of Antwerp) for her expert assistance with FACS experiments. M. Vietri and A. Bellanger (University of Oslo) are acknowledged for providing the RPE-1 2xmRuby3-NES cell line. The plasmid encoding NLS-GFP was a generous gift from J. Goedhart (University of Amsterdam, the Netherlands) and the plasmid encoding RFP-cGAS was kindly provided by J. Lammerding (Cornell University). The plasmids and protocols used for generating the stable HeLa *LMNA* ko cell line were a gift from F. Zhang (Massachusetts Institute of Technology).

Supporting information

One supporting information document that consists of 6 additional figures and 4 supplementary movies are available.

References

1. Purvis, J. E.; Lahav, G. Encoding and Decoding Cellular Information Through Signaling Dynamics. *Cell* **2013,** *152*, 945-956.

2. Ibarra, A.; Hetzer, M. W. Nuclear Pore Proteins and the Control of Genome Functions. *Genes Dev* **2015,** *29*, 337-349.

3. Broers, J. L.; Ramaekers, F. C.; Bonne, G.; Yaou, R. B.; Hutchison, C. J. Nuclear Lamins: Laminopathies and Their Role in Premature Ageing. *Physiol Rev* **2006,** *86*, 967-1008.

4. Lammerding, J.; Schulze, P. C.; Takahashi, T.; Kozlov, S.; Sullivan, T.; Kamm, R. D.; Stewart, C. L.; Lee, R. T. Lamin A/C Deficiency Causes Defective Nuclear Mechanics and Mechanotransduction. *J Clin Invest* **2004,** *113*, 370-378.

5. De Vos, W. H.; Houben, F.; Hoebe, R. A.; Hennekam, R.; van Engelen, B.; Manders, E. M.; Ramaekers, F. C.; Broers, J. L.; Van Oostveldt, P. Increased Plasticity of the Nuclear Envelope and Hypermobility of Telomeres Due to the Loss of A-type Lamins. *Biochim Biophys Acta* **2010,** *1800*, 448-458.

6. Kind, J.; Pagie, L.; de Vries, S. S.; Nahidiazar, L.; Dey, S. S.; Bienko, M.; Zhan, Y.; Lajoie, B.; de Graaf, C. A.; Amendola, M.; Fudenberg, G.; Imakaev, M.; Mirny, L. A.; Jalink, K.; Dekker, J.; van Oudenaarden, A.; van Steensel, B. Genome-Wide Maps of Nuclear Lamina Interactions in Single Human Cells. *Cell* **2015,** *163*, 134-147.

7. De Vos, W. H.; Houben, F.; Kamps, M.; Malhas, A.; Verheyen, F.; Cox, J.; Manders, E. M.; Verstraeten, V. L.; van Steensel, M. A.; Marcelis, C. L.; van den Wijngaard, A.; Vaux, D. J.; Ramaekers, F. C.; Broers, J. L. Repetitive Disruptions of the Nuclear Envelope Invoke Temporary Loss of Cellular Compartmentalization in Laminopathies. *Hum Mol Genet* **2011,** *20*, 4175-4186.

8. Robijns, J.; Molenberghs, F.; Sieprath, T.; Corne, T. D.; Verschuuren, M.; De Vos, W. H. *In Silico* Synchronization Reveals Regulators of Nuclear Ruptures in Lamin A/C Deficient Model Cells. *Sci Rep* **2016,** *6*, 30325.

9. Vargas, J. D.; Hatch, E. M.; Anderson, D. J.; Hetzer, M. W. Transient Nuclear Envelope Rupturing During Interphase in Human Cancer Cells. *Nucleus* **2012,** *3*, 88-100.

10. Denais, C. M.; Gilbert, R. M.; Isermann, P.; McGregor, A. L.; te Lindert, M.; Weigelin, B.; Davidson, P. M.; Friedl, P.; Wolf, K.; Lammerding, J. Nuclear Envelope Rupture and Repair During Cancer Cell Migration. *Science* **2016,** *352*, 353-358.

11. Hatch, E. M.; Hetzer, M. W. Nuclear Envelope Rupture Is Induced by Actin-Based Nucleus Confinement. *J Cell Biol* **2016,** *215*, 27-36.

12. Raab, M.; Gentili, M.; de Belly, H.; Thiam, H. R.; Vargas, P.; Jimenez, A. J.; Lautenschlaeger, F.; Voituriez, R.; Lennon-Dumenil, A. M.; Manel, N.; Piel, M. ESCRT III Repairs Nuclear Envelope Ruptures During Cell Migration to Limit DNA Damage and Cell Death. *Science* **2016,** *352*, 359-362.

13. Maciejowski, J.; Li, Y.; Bosco, N.; Campbell, P. J.; de Lange, T. Chromothripsis and Kataegis Induced by Telomere Crisis. *Cell* **2015,** *163*, 1641-1654.

14. Di Micco, A.; Frera, G.; Lugrin, J.; Jamilloux, Y.; Hsu, E. T.; Tardivel, A.; De Gassart, A.; Zaffalon, L.; Bujisic, B.; Siegert, S.; Quadroni, M.; Broz, P.; Henry, T.; Hrycyna, C. A.; Martinon, F. AIM2 Inflammasome Is Activated by Pharmacological Disruption of Nuclear Envelope Integrity. *Proc Natl Acad Sci U S A* **2016,** *113*, E4671-E4680.

15. Broers, J. L.; Peeters, E. A.; Kuijpers, H. J.; Endert, J.; Bouten, C. V.; Oomens, C. W.; Baaijens, F. P.; Ramaekers, F. C. Decreased Mechanical Stiffness in LMNA-/- Cells Is Caused by Defective Nucleo-Cytoskeletal Integrity: Implications for the Development of Laminopathies. *Hum Mol Genet* **2004,** *13*, 2567-2580.

16. Le Berre, M.; Aubertin, J.; Piel, M. Fine Control of Nuclear Confinement Identifies a Threshold Deformation Leading to Lamina Rupture and Induction of Specific Genes. *Integr Biol (Camb)* **2012,** *4*, 1406-1414.

17. Irianto, J.; Pfeifer, C. R.; Bennett, R. R.; Xia, Y.; Ivanovska, I. L.; Liu, A. J.; Greenberg, R. A.; Discher, D. E. Nuclear Constriction Segregates Mobile Nuclear Proteins Away from Chromatin. *Mol Biol Cell* **2016,** *27*, 4011-4020.

18. Xiong, R.; Raemdonck, K.; Peynshaert, K.; Lentacker, I.; De Cock, I.; Demeester, J.; De Smedt, S. C.; Skirtach, A. G.; Braeckmans, K. Comparison of Gold Nanoparticle Mediated Photoporation: Vapor Nanobubbles Outperform Direct Heating for Delivering Macromolecules in Live Cells. *ACS Nano* **2014,** *8*, 6288-6296.

19. Xiong, R.; Drullion, C.; Verstraelen, P.; Demeester, J.; Skirtach, A. G.; Abbadie, C.; De Vos, W. H.; De Smedt, S. C.; Braeckmans, K. Fast Spatial-Selective Delivery into Live Cells. *J Control Release* **2017,** *266*, 198-204.

20. Saklayen, N.; Huber M.; Madrid M.; Nuzzo V.; Vulis D. I.; Shen W.; Nelson J.; McClelland A. A.; Heisterkamp A.; Mazur E. Intracellular Delivery Using Nanosecond-Laser Excitation of Large-Area Plasmonic Substrates. *ACS Nano* **2017,** 11, 3671-3680.

21. Mobius, W.; van Donselaar, E.; Ohno-Iwashita, Y.; Shimada, Y.; Heijnen, H. F.; Slot, J. W.; Geuze, H. J. Recycling Compartments and the Internal Vesicles of Multivesicular Bodies Harbor Most of the Cholesterol Found in the Endocytic Pathway. *Traffic* **2003,** *4*, 222-231.

22. Tao, J.; Zhang, X. W.; Jin, J.; Du, X. X.; Lian, T.; Yang, J.; Zhou, X.; Jiang, Z.; Su, X. D. Nonspecific DNA Binding of cGAS N-Terminus Promotes cGAS Activation. *J Immunol* **2017,** *198*, 3627-3636.

23. Schmidt, H. B.; Gorlich, D. Transport Selectivity of Nuclear Pores, Phase Separation, and Membraneless Organelles. *Trends Biochem Sci* **2016,** *41*, 46-61.

24. Li, X.; Kang, P.; Chen, Z.; Lal, S.; Zhang, L.; Gassensmith, J. J.; Qin, Z. Rock the Nucleus: Significantly Enhanced Nuclear Membrane Permeability and Gene Transfection by Plasmonic Nanobubble Induced Nanomechanical Transduction. *Chem Commun (Camb)* **2018**, *20*, 2479-2482.

25. Liu, J.; Gaj, T.; Yang, Y.; Wang, N.; Shui, S.; Kim, S.; Kanchiswamy, C. N.; Kim, J. S.; Barbas, C. F. Efficient Delivery of Nuclease Proteins for Genome Editing in Human Stem Cells and Primary Cells. *Nat Protoc* **2015,** *10*, 1842-1859.

26. Yang, Y.; Ren, L.; Wang, H. Strategies in the Design of Gold Nanoparticles for Intracellular Targeting: Opportunities and Challenges. *Ther Deliv* **2017,** *8*, 879-897.

27. Kalderon, D.; Roberts, B. L.; Richardson, W. D.; Smith, A. E. A Short Amino Acid Sequence Able to Specify Nuclear Location. *Cell* **1984,** *39*, 499-509.

28. Yoshida, K.; Seo, H. S.; Debler, E. W.; Blobel, G.; Hoelz, A. Structural and Functional Analysis of an Essential Nucleoporin Heterotrimer on the Cytoplasmic Face of the Nuclear Pore Complex. *Proc Natl Acad Sci U S A* **2011,** *108*, 16571-16576.

29. Suk, J. S.; Xu, Q.; Kim, N.; Hanes, J.; Ensign, L. M. PEGylation as a Strategy for Improving Nanoparticle-Based Drug and Gene Delivery. *Adv Drug Deliv Rev* **2016,** *99*, 28-51.

30. Xiong, R.; Joris F.; Liang S.; De Rycke R.; Lippens S.; Demeester J.; Skirtach A.; Raemdonck K.; Himmelreich U.; De Smedt S. C.; Braeckmans, K. Cytosolic Delivery of Nanolabels Prevents their Asymmetric Inheritance and Enables Extended Quantitative *in Vivo* Cell Imaging. *Nano Lett*, **2016**, *16*, 5975-5986.

31. Jimenez, A. J.; Maiuri, P.; Lafaurie-Janvore, J.; Divoux, S.; Piel, M.; Perez, F. ESCRT Machinery Is Required for Plasma Membrane Repair. *Science* **2014,** *343*, 1247136.

32. Andrews, N. W.; Almeida, P. E.; Corrotte, M., Damage Control: Cellular Mechanisms of Plasma Membrane Repair. *Trends Cell Biol* **2014,** *24*, 734-742.

33. De Vos, W. H.; Hoebe, R. A.; Joss, G. H.; Haffmans, W.; Baatout, S.; Van Oostveldt, P.; Manders, E. M. Controlled Light Exposure Microscopy Reveals Dynamic Telomere Microterritories Throughout the Cell Cycle. *Cytometry A* **2009,** *75*, 428-439.

34. Ran, F. A.; Hsu, P. D.; Wright, J.; Agarwala, V.; Scott, D. A.; Zhang, F. Genome Engineering Using the CRISPR-Cas9 System. *Nat Protoc* **2013,** *8*, 2281-2308.

Graphical Table of Contents